small structures
www.small-structures.com

Cluster-Bridging-Coordinated Bimetallic Metal–Organic Framework as High-Performance Anode Material for Lithium-Ion Storage

Wen Yan, Kun Fan, Li-Min Zheng, and Zhong Jin**

Metal–organic frameworks (MOFs) are potential electrode materials for energy storage owing to abundance of active sites, structural versatility, and well-organized porous framework. Herein, a cluster-bridging-coordinated bimetallic $Co_4(\mu_4\text{-}O)[Ir(ppy\text{-}COO)_3]_2$ MOF (Co_4-Ir MOF) with high conductivity and desirable porosity is proposed as promising anode materials for Li^+ storage. The Co_4-Ir MOF consists of $Co_4(\mu_4\text{-}O)$ clusters bridge-coordinated by $Ir(ppy\text{-}COOH)_3$, leading to electrical conductivity four orders of magnitude higher than that of conventional insulating MOFs and Li^+ diffusion coefficient two orders of magnitude higher than that of graphite, thus boosting rate capability. The laminated stacking structure and ordered porous framework of Co_4-Ir MOF ensure rapid Li^+ transport and storage without large volume variation. As a result, Co_4-Ir MOF anodes deliver high capacity of 1202 mAh g^{-1}, outstanding rate performance (515 mAh g^{-1} at 3000 mA g^{-1}), and good cycling stability (average capacity decay of 0.041% per cycle for 1000 cycles). Soft-packed full batteries assembled with Co_4-Ir MOF anodes and $LiNi_{0.5}Co_{0.2}Mn_{0.3}O_2$ cathodes exhibit good stability and flexibility. Moreover, Co_4-Ir MOF anode with fast kinetics is applied in hybrid lithium-ion capacitor, demonstrating good compatibility with capacitor-type cathode. This work suggests great potential to rationally design MOF materials with intriguing structures and performances for sustainable energy storage applications.

1. Introduction

Lithium-ion batteries (LIBs) have been widely used as power sources for electric vehicles and portable electronics.[1–4] Commercial graphite anodes deliver a low theoretical capacity of 372 mAh g^{-1} and suffer from sluggish reaction kinetics, which is a major restriction for improving the energy density and rate performance of LIBs.[5,6] Extensive efforts have been dedicated to developing desirable anode materials with high capacity, rate capability, and cycling stability. Transition metal oxides/sulfides/nitrides,[7–10] Si-based composites,[11–14] and carbonaceous materials[15–18] have attracted considerable interest as potential anode materials due to their high capacity. However, the large volume variation that occurs during the lithiation/delithiation processes renders the solid-electrolyte interphase (SEI) unstable and leads to pulverization of the electrode, which could result in fast capacity degradation of the battery.[19,20] Thus, the rational design of anode materials with high capacity and long-term cycling stability is an ongoing challenge.

Metal–organic frameworks (MOFs) are composed of tunable metal centers and organic ligand building blocks, exhibiting high crystallinity and ordered porosity.[21] Recently, the probability of utilizing pristine MOFs as active materials in the anodes of LIBs has been investigated.[22–31] To date, two main types of lithiation/delithiation mechanisms in pristine MOF anode materials have been proposed: 1) "metal-dominated" mechanism involving the conversion reaction of metal ions, such as $Mn[Fe(CN)_6]_{0.6667}\cdot nH_2O$,[23] Mn-LCP,[26] and NNU-11[27]; and 2) "organic-dominated" mechanism with Li^+ intercalation/deintercalation, such as 2,6-naph$(COOLi)_2$,[22] Cu-BTC,[24] and $Co_2(OH)_2BDC$.[25] The MOF anode materials with a "metal-dominated" mechanism exhibit a constant voltage plateau with one or more electrons stored per unit, but they deliver limited specific capacities in view of their large molecular masses. Moreover, the coordination network of these MOFs may be destroyed during the lithiation/delithiation processes, thus leading to poor cycling stability.[32] In contrast, the MOF anode materials with an "organic-dominated" mechanism are based on Li^+ insertion into organic moieties, and the main active sites for storing Li^+ ions are attributed to carboxyl groups, benzene rings,

W. Yan, K. Fan, L.-M. Zheng, Z. Jin
State Key Laboratory of Coordination Chemistry
MOE Key Laboratory of Mesoscopic Chemistry
MOE Key Laboratory of High Performance Polymer Materials and Technology
Jiangsu Key Laboratory of Advanced Organic Materials
School of Chemistry and Chemical Engineering
Nanjing University
Nanjing, Jiangsu 210023, China
E-mail: lmzheng@nju.edu.cn; zhongjin@nju.edu.cn

W. Yan, Z. Jin
Shenzhen Research Institute of Nanjing University
Shenzhen 518063, China

W. Yan
School of Chemistry and Materials Science
Jiangsu Normal University
Xuzhou, Jiangsu 221116, China

The ORCID identification number(s) for the author(s) of this article can be found under https://doi.org/10.1002/sstr.202100122.

DOI: 10.1002/sstr.202100122

pore channels, and/or interlamination space.[22,25] In the case of MOFs with an "organic-dominated" mechanism, the voltage profile shows a sloping curve without a definitive plateau. Moreover, these MOFs exhibit exceptional specific capacities owing to the abundance of accessible active sites for lithiation/delithiation.[32] However, the intrinsically low bulk conductivity of conventional MOFs, originating from the insulating nature of organic linkers and the poor electron transfer between organic linkers and metal clusters, hinders their application in high-rate performance LIBs. Therefore, the integration of both high-energy density and high conductivity into MOF materials is a promising but challenging route to achieve fast and high-power energy storage. Tailoring the components and topological structures of MOFs, such as constructing bimetallic MOFs[31,33] and two-dimensional conjugated MOFs with layer stacks,[34–41] are promising routes to achieve both high-energy density and enhanced conductivity.

Herein, we report the development of a cluster-bridging-coordinated bimetallic $Co_4(\mu_4\text{-O})[Ir(ppy\text{-}COO)_3]_2$ MOF (Co_4-Ir MOF) consisting of $[Ir(ppy\text{-}COOH)_3]$ metallolinkers [ppy-COOH = 3-(pyridin-2-yl)benzoic acid] and cobalt(II) ion nodes as the anode material for LIBs. The bimetallic Co_4-Ir MOF with a laminated stacking structure exhibits greatly enhanced electrical conductivity and ion transport capability compared to conventional monometallic MOFs, which is very helpful for achieving LIBs with high-rate performance. The electrochemical performance of the Co_4-Ir MOF anode is investigated, exhibiting remarkably high discharge capacity, rate performance, and long-term cycling stability. *Ex situ* characterizations verify the "organic-dominated" mechanism of Co_4-Ir MOF in the lithiation/delithiation processes and the buffering of the volume expansion/contraction during cycling. Furthermore, soft-packed full batteries based on Co_4-Ir MOF anodes and commercial $LiNi_{0.5}Co_{0.2}Mn_{0.3}O_2$ (NCM523) cathodes also achieve good cycling stability and mechanical flexibility.

2. Results and Discussion

The cluster-bridging-coordinated bimetallic Co_4-Ir MOF was prepared by the solvothermal reaction of $Co(NO_3)_2{\cdot}6H_2O$ and $Ir(ppy\text{-}COOH)_3$ [ppy-COOH = 3-(pyridin-2-yl)benzoic acid] in a solution of $DMF/H_2O/HCl$ (**Figure 1**a). Single-crystal X-ray analyses reveal that the Co_4-Ir MOF crystallizes in a triclinic crystal system with *R3* space group (Tables S1 and S2, Supporting Information). The molecular structure of Co_4-Ir MOF (Figure 1b) is formed of one-third $Ir(ppy\text{-}COOH)_3$, two-thirds Co centers, and one-sixth μ_4-O atom in an asymmetric unit. An interesting feature of this structure is the presence of a unique $Co_4(\mu_4\text{-O})$ cluster where eight Co atoms form two regular tetrahedral structures due to the positional disorder of Co^{2+} ions, which has been reported in Zn-based MOFs but has never been reported in Co-based MOFs.[42–44] The bond lengths of $Co{-}O_{center}$ (1.851 and 1.973 Å) are slightly smaller than the $Co{-}O_{carboxylate}$ bond lengths (2.066–2.189 Å). The Co_4-Ir MOF shows a two-dimensional layered structure, in which metalloligand $Ir(ppy\text{-}COOH)_3$ serves as a linker to chelate and bridge the $Co_4(\mu_4\text{-O})$ units to form a layer, which is similar to the isomorphic structure of Zn_4-Ir MOF.[42,45] These layers are connected by π–π stacking and are packed along the c-axis with the closest interlayer distance being 3.6 Å, thus a three-dimensional supramolecular network containing open channels with sizes of 5.8×3.6 Å is successfully formed. As illustrated in the PXRD patterns (Figure S1, Supporting Information), HCl plays a key role in the crystallization, a small amount of HCl can slow down the nucleation rate and lead to single crystals. However, if too much HCl was added, the powder or even other impurities will be obtained. Given the degree of crystallinity and the production yield, 23 μL of HCl was proved as the optimal quantity.

Scanning electron microscopy (SEM) image of Co_4-Ir MOF shows a hexagonal plate-like shape (Figure 1c), indicating its high crystallinity and laminated stacking structure. Energy-dispersive X-ray (EDX) spectroscopy analysis confirms the presence of Co, O, C, N, and Ir elements (Figure S2, Supporting Information). The Fourier transform infrared (FTIR) spectrum of $Ir(ppy\text{-}COOH)_3$ shows a characteristic band located at around 1446 cm^{-1}, which is attributed to the asymmetric stretching of −COOH. This peak disappears in the FTIR spectrum of Co_4-Ir MOF, indicating the deprotonation of the $Ir(ppy\text{-}COOH)_3$ ligand when coordinating with $Co_4(\mu_4\text{-O})$ cluster (Figure 1d). The broad absorption peak at 3440 cm^{-1}, which represents O–H stretching vibration, confirms the presence of water in the framework. Moreover, absorption peaks at 2950, 2925, and 2850 cm^{-1} also indicate the existence of DMF in the pores and channels of Co_4Ir MOF crystal. The as-measured powder X-ray diffraction (PXRD) pattern of Co_4-Ir MOF is identical to that simulated from the single-crystal data, showing a high degree of crystallinity (Figure 1e). Due to the severe disorder of lattice solvent molecules, the contents and locations of water and DMF in Co_4-Ir MOF cannot be modeled in the single-crystal X-ray analysis. The total number of lattice solvent molecules in the molecular formula was confirmed on the basis of both elemental and thermal analyses (Figure S2 and S3, Supporting Information). According to thermogravimetric analysis (TGA), Co_4-Ir MOF first loses its weight below 100 °C, corresponding to the evaporation of adsorbed water. Then, the adsorbed DMF solvent starts to evaporate at ≈150 °C (Figure S3, Supporting Information). The contents of adsorbed water and DMF were calculated to be 9.5 and 11.9 wt% in the Co_4-Ir MOF crystal, suggesting a molecular formula of $\{Co_4(\mu_4\text{-O})[Ir(ppy\text{-}COO)_3]_2\}{\cdot}4DMF{\cdot}12H_2O$. Before assembling the batteries, the anode containing active material Co_4-Ir MOF was dried under vacuum at 100 °C overnight. The weight loss of Co_4-Ir MOF anode is 21.7 wt% after heat treatment, which is in consistent with the mass ratio of water and DMF (21.4 wt% in TGA analysis). Besides, FTIR spectrum of Co_4-Ir MOF anode was further measured to verify the complete removal of lattice solvents (Figure 1d and S4, Supporting Information). The peaks assigned to water (3440 cm^{-1} in Figure 1d) and DMF (2950, 2925, 2850 cm^{-1} in Figure S4, Supporting Information) are absent in the Co_4-Ir MOF anode, indicating the complete removal of solvents in the electrode preparation process. The N_2 adsorption and desorption isotherm of Co_4-Ir MOF at 77 K shows a type I curve with a specific surface area of 703 $m^2\,g^{-1}$ (Figure 1f), which is typical for microporous materials. The pore size distribution determined by the Horvath–Kawazoe (HK) method is 0.51 nm (Figure 1g), which matches well with the crystal structure of Co_4-Ir MOF. Co with valence electron structure of $[3d^74s^2]$ has high coordination number when it is chelated with diverse

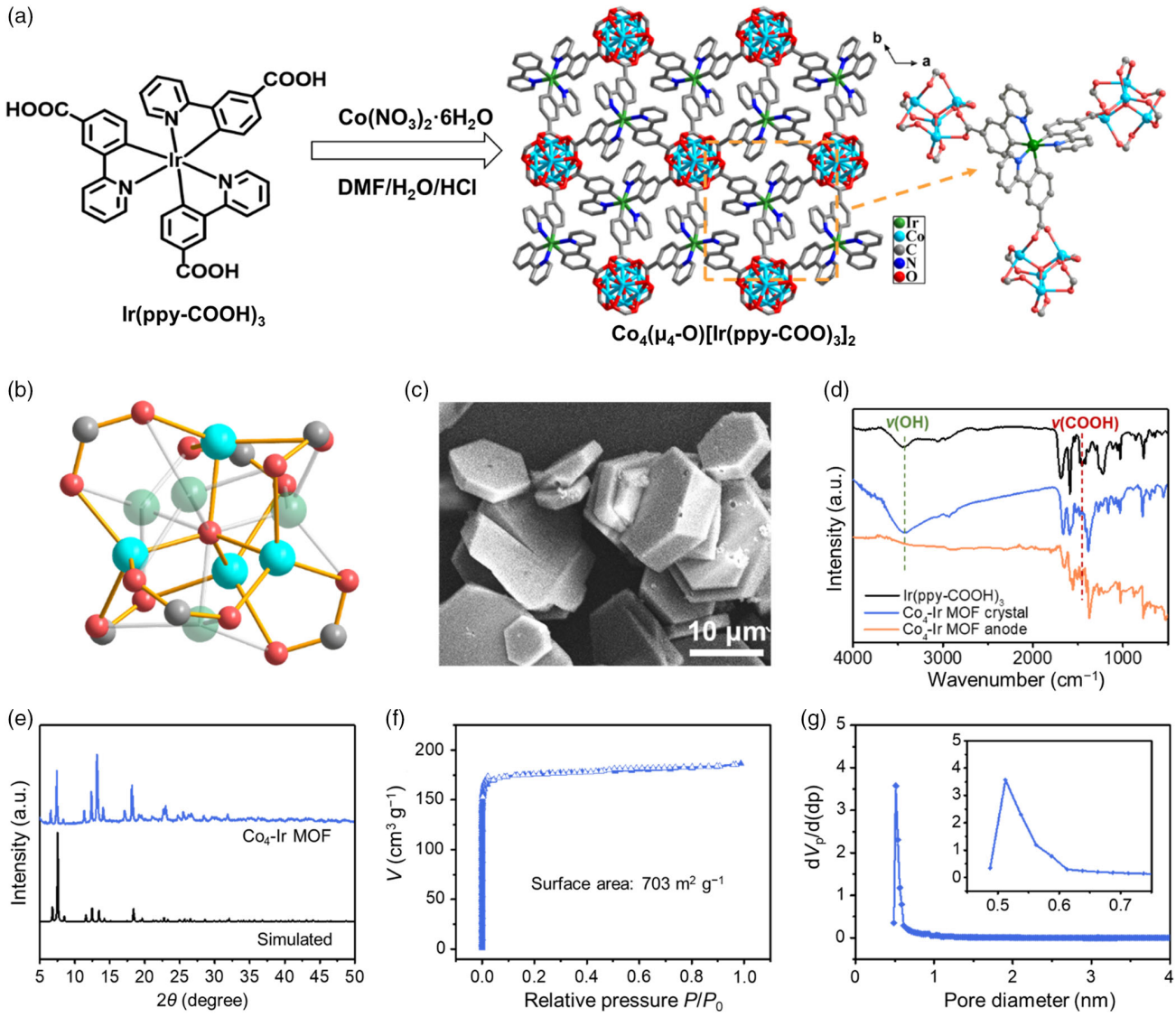

Figure 1. Synthesis and characterizations of Co_4-Ir MOF. a) Schematic preparation process and structural configuration of Co_4-Ir MOF. b) Coordination environment of the Co^{II} ions in $Co_4(\mu_4\text{-O})$ cluster. c) SEM image of Co_4-Ir MOF. d) FTIR spectra of Ir(ppy-COOH)$_3$ ligand, Co_4-Ir MOF crystal, and Co_4-Ir MOF anode. e) Measured and simulated PXRD patterns of Co_4-Ir MOF. f) Nitrogen adsorption and desorption isotherm and g) Horvath–Kawazoe (HK) pore size distribution of Co_4-Ir MOF at 77 K.

ligands, which ensures desirable chemical and thermal stability of Co-based MOFs. Moreover, Co-O clusters in Co-based MOFs could participate in the electrochemical reaction to interact with Li^+ ions due to weak electron-withdrawing property of carboxylates.[46] Therefore, Co-based MOFs are extensively utilized as electrode materials for advanced energy storage applications.[47,48] To promote the electron transport of MOFs, ligands with distance-dependent π–π interaction and large π-conjugated aromatic systems are encouraged.[49] Herein, Ir(ppy-COOH)$_3$ metallolinkers chelate and bridge the $Co_4(\mu_4\text{-O})$ units to form π–π stacking layers. On the other hand, the highly connected Ir atoms ensure the formation of robust bimetallic frameworks. As a result, the bulk electrical conductivity of the bimetallic Co_4-Ir MOF is measured to be 5.6×10^{-4} S m^{-1} (Figure S5, Supporting Information), four orders of magnitude higher than that of conventional insulated MOFs ($<10^{-8}$ S m^{-1}), which is very conducive to the high-rate capability of LIBs.[50,51]

The electrochemical performance of Co_4-Ir MOF was first investigated using a half-cell configuration with Li metal as the counter electrode. **Figure 2**a shows the cyclic voltammetry (CV) curves of Co_4-Ir MOF anode with an areal mass loading of 2.0 mg cm^{-2} at 1 mV s^{-1}. The peak appearing at 0.57 V in the 1st negative sweep but disappearing in the following cycles is mainly ascribed to the formation of the SEI due to the decomposition of carbonate electrolyte.[28] From the 2nd cycle, instead of sharp peaks, broad anodic and cathodic peaks are observed in the CV curves, indicating gradual multistep Li^+ insertion/extraction processes. As Li^+ infuses into active sites, including

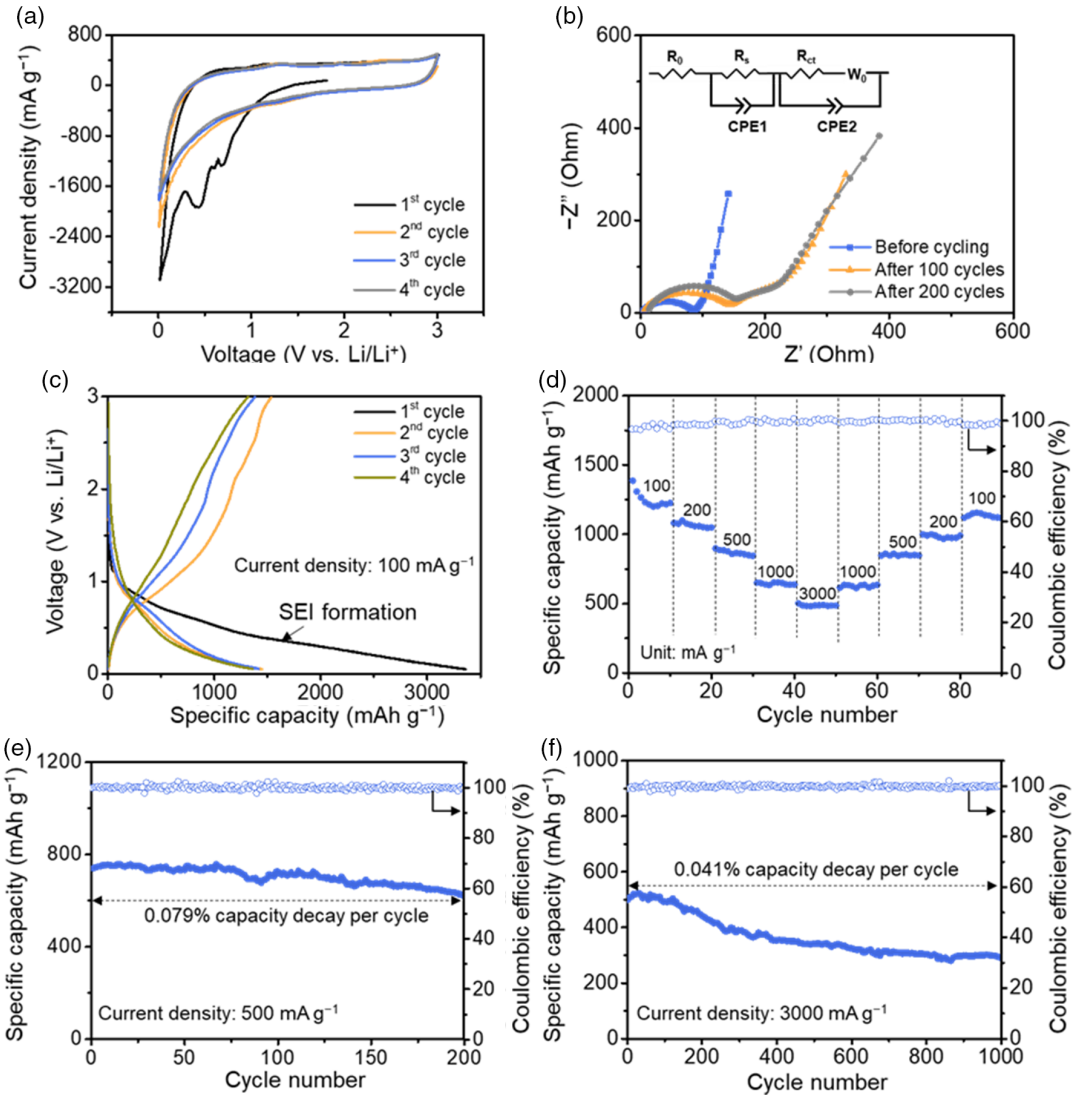

Figure 2. Electrochemical performance of Co_4-Ir MOF anode. a) CV curves of Co_4-Ir MOF anode at a scan rate of 1 mV s^{-1}. b) EIS curves of Co4-Ir MOF anode at the fresh state and after cycling. c) Galvanostatic charge–discharge curves of Co_4-Ir MOF anode at a current density of 100 mA g^{-1}. d) Rate performance of Co_4-Ir MOF anode from 100 to 3000 mA g^{-1}. e,f) Long-term stability of Co_4-Ir MOF anode at the current densities of 500 mA g^{-1} and 3000 mA g^{-1}, respectively.

aromatic rings, carboxyl groups, Co_4O inorganic clusters, pore channels, and the interlamination space, there will be an increasing repulsion between charges, leading to the absence of any sharp peaks.[52,53] The CV curves in the 3rd and 4th cycles overlap well with that of the 2nd cycle, indicating the high reversibility of Li^+ insertion/extraction. Electrochemical impedance spectroscopy (EIS) measurements were performed in the frequency range of 0.01 Hz–100 kHz. As depicted in Figure 2b, the EIS spectrum is composed of a semicircle at high/middle frequency and a linear part at low frequency. The small semicircle at the high/middle frequency suggests rapid charge transfer during the electrochemical process. The cycling behavior of Co_4-Ir MOF anode was evaluated at 100 mA g^{-1} in the voltage range from 0.05 to 3.0 V *versus* Li/Li$^+$. As shown in Figure 2c, the Co_4-Ir MOF anode exhibits a discharge capacity of 3360 mAh g^{-1} in the first cycle. The irreversible capacity in the first cycle was ascribed to the formation of an SEI layer and the lithiation of the Co_4-Ir MOF anode.[24] The discharge capacities at the 2nd, 3rd, and 4th cycles are 1450, 1420, and 1380 mAh g^{-1} with Coulombic efficiencies of 94.9%, 97.1%, and 97.3%, respectively. Figure 2d and S6, Supporting Information, display the rate performance of the Co_4-Ir MOF anode from 100 to 3000 mA g^{-1}. The Co_4-Ir MOF anode achieves average discharge capacities of 1202, 1059, 866, 653, and 487 mAh g^{-1} with Coulombic efficiencies approaching 100% at various current densities of 100, 200, 500, 1000, and 3000 mA g^{-1}, respectively. Notably, the specific capacity can be recovered to 1155 mAh g^{-1} when the current density is reduced back to 100 mA g^{-1}, demonstrating the good reversibility of Co_4-Ir MOF anode. To study the long-term cycling stability, a Co_4-Ir

MOF||Li half-cell was cycled at a current density of 500 mA g^{-1} (Figure 2e), showing an initial discharge capacity of 740 mAh g^{-1} and a Coulombic efficiency of 99.75%. After 200 cycles, a specific capacity of 623 mAh g^{-1} is still maintained, corresponding to a capacity retention of 84.2%. The EIS tests of the cycled cells after different cycle numbers indicate the interfacial evolution of the Co_4-Ir MOF anode (Figure 2b). It is conjectured that the increase of resistance is owing to the growth of SEI layer on the anode. Note that the resistance keeps almost constant after cycling for 200 cycles, suggesting a stable electrode/electrolyte interface and high Li ion diffusivity. When tested at an ultrahigh current density of 3000 mA g^{-1}, the Co_4-Ir MOF anode exhibits an initial capacity of 497 mAh g^{-1} and an average capacity decay of 0.041% per cycle for 1000 cycles. This outstanding rate performance and cycling stability of the Co_4-Ir MOF are competitive among previously reported pristine MOF anodes (Table S3, Supporting Information).[22–31] The high surface area of the nanostructural materials results in unstable solid-electrolyte interfaces (SEI) and successive consumption of electrolyte, which is the potential reason for the capacity decay of MOFs. We suggest that the cycling stability of MOFs could be further improved by tuning their sizes, microstructures, and compositions, as well as adding proper electrolyte additives to enhance the stability of SEI film and reduce the electrolyte consumption. Further investigation on the improvement of the battery performance by finely tailoring the topological structure of MOFs and regulating the SEI formation will be an important aspect of our future research.

To further understand the charge-storage kinetics of Co_4-Ir MOF anode, CV measurements were conducted at scan rates from 0.2 to 10.0 mV s^{-1} (**Figure 3**a). The *b*-value was calculated to distinguish the capacitive contribution according to the following equations[54]

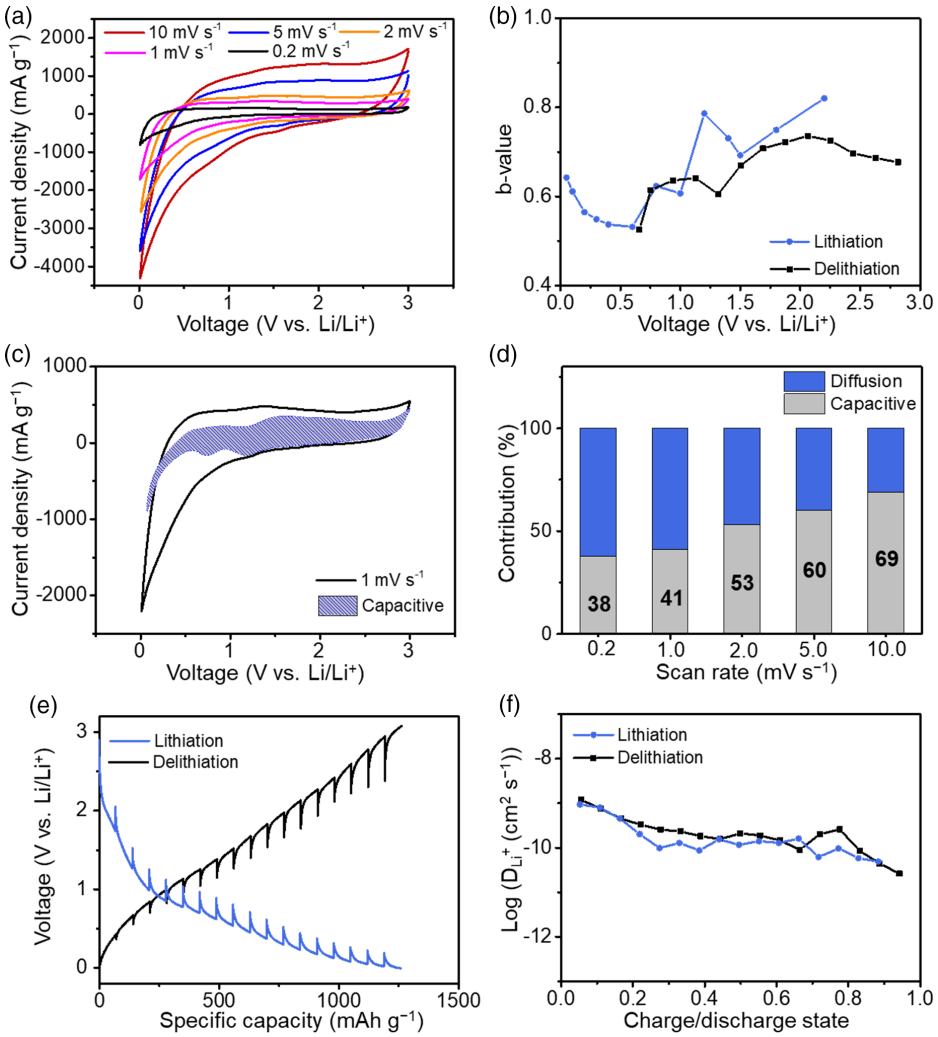

Figure 3. Electrochemical kinetic properties of Co_4-Ir MOF anode. a) CV curves at various scan rates from 0.2 to 10.0 mV s^{-1}. b) Calculated *b*-values as a function of voltage for the cathodic and anodic processes. c) CV curves at a scan rate of 1.0 mV s^{-1}. The capacitive contribution is marked by the blue shaded region. d) Normalized contribution ratios of the pseudocapacitive process to the total capacity at different scan rates. e) GITT curves of the Co_4-Ir MOF anode at a constant current density of 50 mA g^{-1} with a relaxation time of 30 min. f) Logarithm of the calculated Li^+ diffusion coefficients for the lithiation and delithiation processes.

$$i(V) = av^b \quad (1)$$

$$logi(V) = blogv + loga \quad (2)$$

where $i(V)$ is the current at certain potentials (V), *versus* is the scan rate, and a and b are adjustable parameters. The b-value can be determined by plotting $logi(V)$ versus $logv$. The electrode kinetics are controlled by the diffusion process when the b-value is 0.5, while the surface capacitive process dominates when the b-value approaches 1.0. As shown in Figure 3b, the b-values vary with the charge/discharge state, suggesting different capacitive contributions during the lithiation/delithiation process. When inserting Li^+ in the Co_4-Ir MOF anode, the average b-value is 0.76 in the range of $1.2 - 2.2$ V *versus* Li/Li^+, indicating that capacitive behavior dominates within this voltage range. The b-value then decreases to 0.58, indicating that Li^+ intercalation dominates the electrochemical process within 0.1–1.0 V *versus* Li/Li^+. The average b-value for the delithiation process is 0.67, which suggests that both the capacitive and diffusion-controlled processes contribute to the total capacity. As shown in Figure 3c,d, the capacitive contributions are calculated to be 38%, 41%, 53%, 60%, and 69% at the scan rates of 0.2, 1.0, 2.0, 5.0, and 10.0 mV s^{-1}, respectively. This result suggests that the capacity of Co_4-Ir MOF anode is contributed by both pseudocapacitive processes (accounting for the high rate capability) and intercalation reactions (contributing to the high specific capacity). The self-discharge behavior of the Co_4-Ir MOF anode was also examined, as shown in Figure S7, Supporting Information. Time-dependent voltage changes beginning from a state-of-charge (SOC) of 100% (fully charged) were recorded for 48 h (Figure S7a, Supporting Information), showing that 97.5% of the original capacity is still maintained after 48 h (Figure S7b, Supporting Information), thus proving the low self-discharge rate and remarkable stability of Co_4-Ir MOF anode. The Li^+ diffusion coefficient ($D_{Li}{}^+$) of the Co_4-Ir MOF anode was evaluated by the galvanostatic intermittent titration technique (GITT). The charged and discharged GITT curves were measured at a current density of 50 mA g^{-1} for 20 min followed by a rest time of 30 min to reach the steady-state voltage (Figure 3e). The $D_{Li}{}^+$ at various charge/discharge states calculated from the GITT curves are profiled in Figure 3f, exhibiting values of $2.62 \times 10^{-11} \approx 1.20 \times 10^{-9}$ cm^2 s^{-1}. The $D_{Li}{}^+$ of Co_4-Ir MOF is two orders of magnitude higher than that of graphite, which is beneficial to achieving LIBs with high-rate capability. Generally, the Li-ion diffusivity in the Co_4-Ir MOF anode is competitive with that of anodes from other reported works.[50]

To clarify the lithiation–delithiation mechanism in Co_4-Ir MOF anodes, *ex situ* characterizations of pristine, fully charged (delithiation) and fully discharged (lithiation) anodes, were conducted (**Figure 4**). The PXRD patterns show that Co_4-Ir MOF well maintained its original framework integrity after cycling (Figure 4b). As illuminated in the *ex situ* FTIR results for Co_4-Ir MOF anode (Figure 4c), several bands at 1646, 1575, and 1507 cm^{-1} can be assigned to the C═O groups and the aromatic C═C groups, respectively. It can be observed that the bands of C═O and C═C groups become weaker in the lithiation process, while it recovers during the following delithiation process. It indicates the reversible Li ion interaction with the unsaturated carbons of Co_4-Ir MOF, which has also been shown in conjugated aromatic compounds.[52,55,56] *Ex situ* XPS spectra were also conducted to monitor the component variation of Co_4-Ir MOF anode. The survey XPS spectrum of pristine Co_4-Ir MOF shows the coexistence of Co, O, C, N, and Ir elements (Figure S8, Supporting Information), consistent with the EDX result (Figure S2, Supporting Information).The high-resolution C 1s spectrum of pristine Co_4-Ir MOF exhibits six deconvolution peaks at 289.2, 287.5, 286.7, 286, 285.2, and 284.5 eV, corresponding to the COO, C—O, C═N, C—N, C—C, and C═C bonds, respectively (Figure 4d). The emerging peaks at 290.0 eV in the C 1s spectra (Figure 4d) and 55.0 eV in the Li 1s spectra (Figure 4f) after cycling are assigned to the Li_2CO_3. Due to the formation of SEI film on the outer surface of anode, the intensities of Co 2p (Figure 4e) and Ir 4f (Figure 4f) peaks decrease, and the intensity of O 1s (Figure 4g) peak increases, compared with that of the pristine sample. The area ratio of the peaks for C—C and C═C groups increases during the lithiation process and then recovers in the following delithiation process (Figure 4d), indicating the reversible transformation between C═C and C—C groups in benzene rings. The binding energy of Ir 4f shifts to lower binding energies in the lithiation process and recovers after delithiation, suggesting the coordination environment of Ir center varies with interactions between Li ions and unsaturated carbon in $Ir(ppy\text{-}COO)_3$ ligand.[57] No discernible peak location changes are observed in the Co 2p spectra after cycling, indicating the absence of any Co(0) species after fully discharging. These results clearly confirm the stable structure integrity of Co_4-Ir MOF and the "organic moiety-dominated" mechanism during the cycling processes. As depicted in Figure 4a, besides possible lithiation sites at C═O group and Co_4O inorganic cluster, Li ions can be stored on the unsaturated carbons of aromatic rings. In the lithiation process (Figure S9, Supporting Information), the bump at ≈1.2 V is related to the reduction of C═O group and Li^+ intercalation into Co_4O inorganic clusters. The subsequent sharp current declination from 0.8 to 0.05 V is ascribed to Li^+ intercalation into the aromatic rings in organic ligands, which accounts for most of the capacity. Besides, Li^+ filling/plating in micropores or mesopores of MOFs also contributes to the capacity in the lithiation process. On the reverse delithiation sweep, a current hump extending to ≈1.0 V corresponds to the extraction process of Li^+ ions from lithiated Co_4-Ir MOF step by step. The subsequent peak at ≈1.3 V could be attributed to the recovery of C═O bonds with the extraction of Li^+ ions from Co_4O clusters. The increased current response from 2.5 to 3.0 V corresponds to the intercalation of $PF_6{}^-$ anions.[57] Due to the repulsion between charges, no obvious plateau can be observed in the voltage profiles. Based on the proposed mechanism, a maximum of 88 Li^+ per unit ($C_{72}H_{42}Co_4Ir_2N_6O_{13}$) are involved in the electrochemical process of Co_4-Ir MOF, which matches with the reversible capacity of 1200 mAh g^{-1}.

To further explore the practical performance of Co_4-Ir MOF anodes in LIBs, we also assembled soft-packed full batteries with Co_4-Ir MOF anodes and NCM523 cathodes (**Figure 5**a). The specific capacity was calculated based on the mass of Co_4-Ir MOF. The soft-packed Co_4-Ir MOF||NCM523 batteries deliver an initial discharge capacity of 352 mAh g^{-1} with an average voltage plateau of 3.90 V (Figure 5b,c). The energy density of Co_4-Ir MOF||NCM523 full cell is estimated to be 301 Wh kg^{-1} on the basis of the total mass of cathode and anode. Figure 5c presents

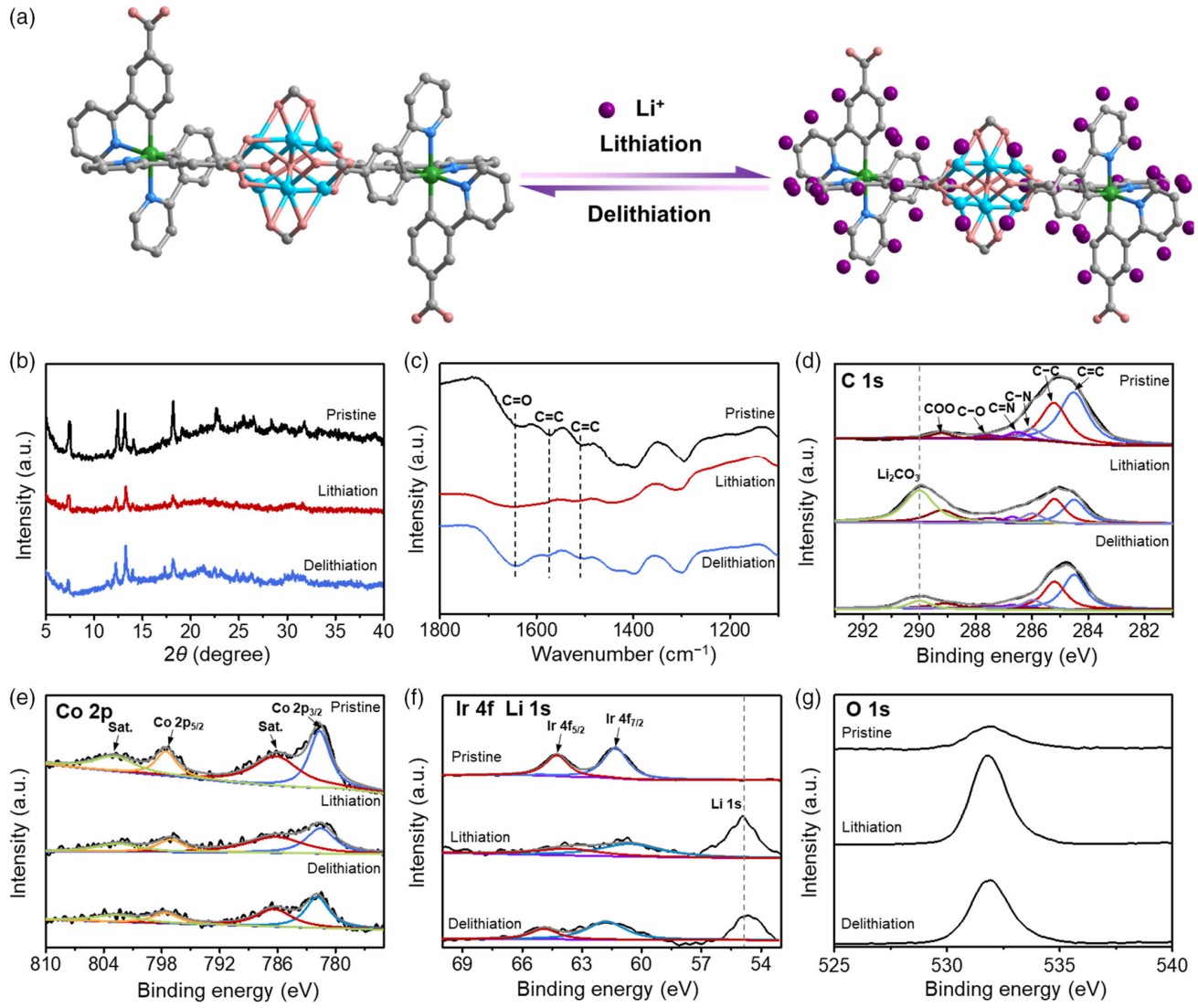

Figure 4. Li ion storage mechanism of Co_4-Ir MOF. a) Schematic diagram for the proposed active sites in Co_4-Ir MOF during the lithiation/delithiation processes. b) *Ex situ* XRD patterns and c) *Ex situ* FTIR spectra of Co_4-Ir MOF anodes at pristine state (black line), fully discharged state (red line), and fully charged state (blue line), respectively. High-resolution XPS spectra of Co_4-Ir MOF anode in the d) C 1s region, e) Co 2p region, f) Ir 4f and Li 1s regions, and g) O 1s region.

the galvanostatic charge–discharge curves of the full battery at 100 mA g^{-1} in a voltage window of 1.0–4.2 V. The full battery exhibits good stability with a remaining specific capacity of 246 mAh g^{-1} after 35 cycles under continuous bending–unbending operation. As shown in Figure 5d, the soft-packed Co_4-Ir MOF||NCM523 battery can be used to power LEDs during continuous bending–unbending processes. The light intensity of the LEDs exhibits no visual disparity, suggesting the stable electrochemical performance and high flexibility of the full battery under dynamic conditions. The Co_4-Ir MOF||NCM523 full cell delivers capacity of 147 mAh g^{-1} after 200 cycles at 1000 mA g^{-1} with Columbic efficiency around 100% (Figure 5e).

The Co_4-Ir MOF anode with fast kinetics also exhibits good compatibility with capacitor-type cathodes in hybrid lithium-ion capacitors (HLICs). To explore the electrochemical performance of Co_4-Ir MOF anodes in HLICs, we assembled full-cell HLICs with Co_4-Ir MOF anodes and activated carbon (AC) cathodes. The electrochemical performance of AC cathode in a Li half-cell configuration was also evaluated by galvanostatic charging–discharging processes. (Figure S10, Supporting Information) The specific capacities of AC cathode are 58, 55, 48, 42, and 32 mAh g^{-1} at 100, 500, 1000, 2000, and 4000 mA g^{-1}, respectively. For Co_4-Ir MOF anode, the specific capacity is 180 mAh g^{-1} even at a high current density of 4000 mA g^{-1}. To ensure optimal cell performance, the capacity ratio of the anode and cathode materials was balanced to be 1.1:1. Therefore, the mass ratio of Co_4-Ir MOF to AC was approximately 1:5. **Figure 6**a shows the CV curves of HLICs at different scan rates. The quasi-rectangular current response in CV curves suggests the electrochemical kinetics balance of the Co_4-Ir MOF

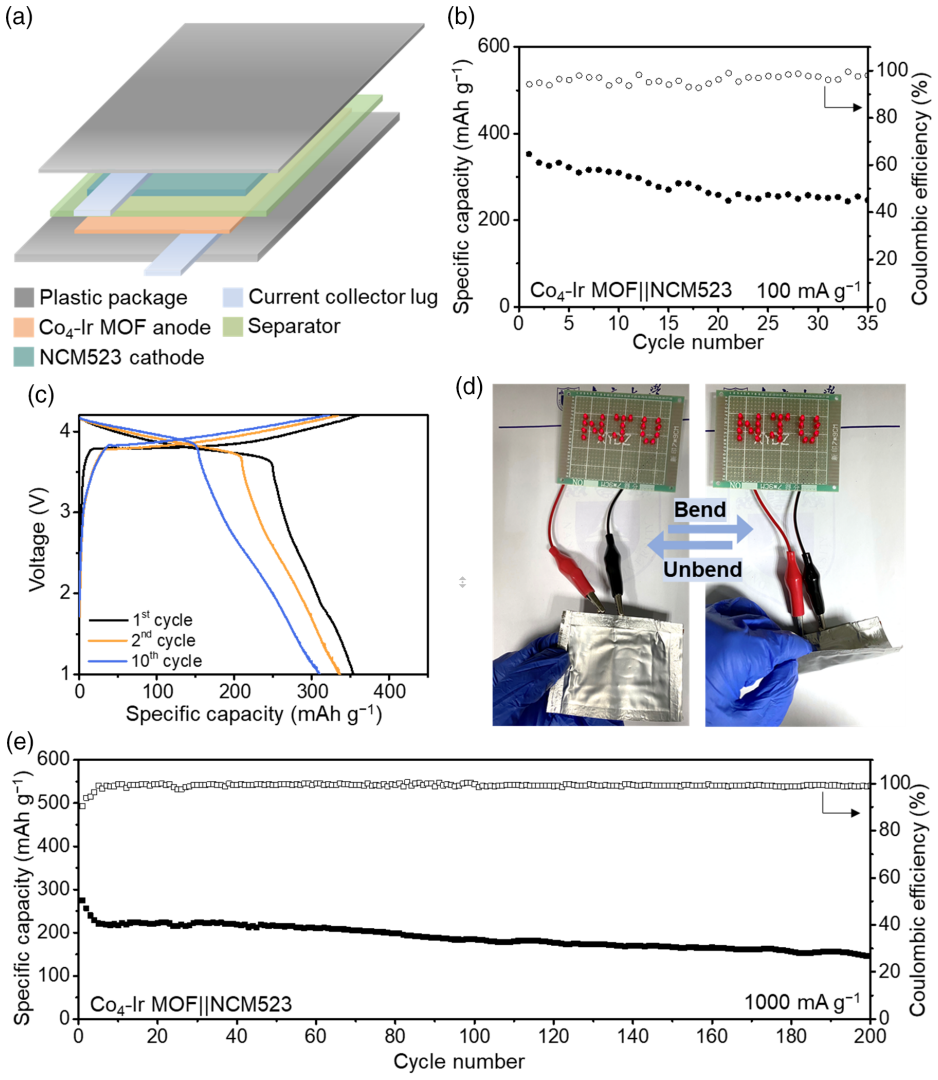

Figure 5. a) Schematic illustration of a soft-packed full battery assembled with the Co_4-Ir MOF anode and an NCM523 cathode. b) Cycling performance and c) galvanostatic charge–discharge curves of the soft-packed battery at a current density of 100 mA g^{-1} under continuous bending-unbending operation. d) Optical images with a pattern of "NJU" consisting of 25 LEDs simultaneously lit by the full battery under continuous bending and unbending operation. e) Long-term cycling stability of Co_4-Ir MOF||NCM523 full cell at a current density of 1000 mA g^{-1}.

anode and AC cathode. Figure 6b presents the galvanostatic charge–discharge voltage profiles of the Co_4-Ir MOF||AC HLICs in the range of 2.0–4.0 V at different current densities. The nearly triangular voltage profiles indicate ideal capacitive behavior. The specific capacitances are calculated to be 59, 45, 38, 33, 28, and 24 F g^{-1} at the current densities of 100, 200, 500, 1000, 2000, and 4000 mA g^{-1}, respectively. The Ragone plots of the Co_4-Ir MOF||AC HLICs obtained by calculating the energy density and power density at different current densities are shown in Figure 6c, delivering a high-energy density of 165.4 Wh kg^{-1} at 300 W kg^{-1} and a high-power density of 12 000 W kg^{-1} at 53.7 Wh kg^{-1}. The outstanding energy density, power density, and lifespan of the Co_4-Ir MOF||AC HLIC are competitive among the previously reported HLICs with MOF-based anode materials (Figure 6c).[29,30,58–60] The cycling stability of HLICs was evaluated by long-term cycling experiments at 4000 mA g^{-1}, showing a high capacity retention of 73.6% after 3000 cycles.

3. Conclusion

In summary, we report the design and synthesis a cluster-bridging-coordinated bimetallic Co_4-Ir MOF and investigated its Li^+ storage behavior in detail as a promising large-capacity and high-rate anode for LIBs and HLICs. *Ex situ* characterizations demonstrate that the reversible Li^+ storage behavior of Co_4-Ir MOF anode is based on "organic-dominated" mechanism where Li^+ ions are reversibly inserted into/extracted from organic sites, such as carboxyl groups, benzene rings, pore channels, and/or interlamination space. Moreover, the laminated stacking structure and well-organized porous framework of

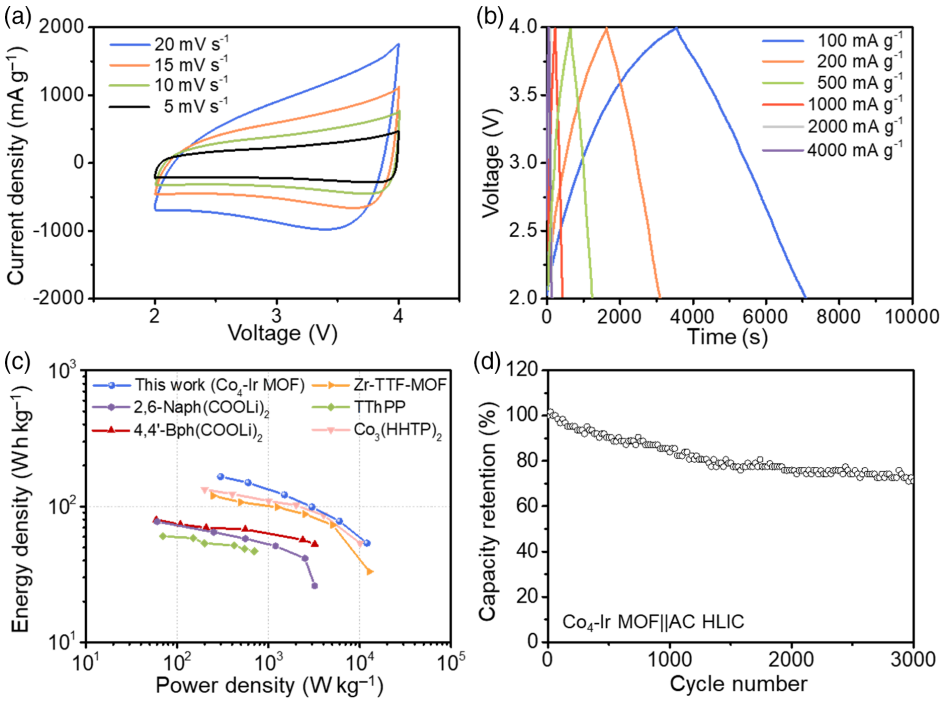

Figure 6. Electrochemical performance of Co_4-Ir MOF||AC HLICs. a) CV curves of HLICs between 2.0 and 4.0 V at various scan rates from 5 to 20 mV s^{-1}. b) Galvanostatic charge–discharge curves of HLICs at different current densities from 100 to 4000 mA g^{-1}. c) Ragone plots of Co_4-Ir MOF||AC HLICs in this work compared with other representative HLICs involving pristine MOF anode materials.[29,30,58–60] d) Long-term stability of HLICs at a current density of 4000 mA g^{-1}.

Co_4-Ir MOF ensure improved Li^+ transport and storage without large volume expansion/contraction during cycling. Benefitting from its high intrinsic conductivity and abundant active sites for Li^+ storage, the Co_4-Ir MOF anode delivered a high reversible capacity (1202 mAh g^{-1} at 100 mA g^{-1}), outstanding rate capability (515 mAh g^{-1} at 3000 mA g^{-1}), and stable cycling performance (84.2% capacity retention after 500 cycles). This work provides an intriguing paradigm for broadening the design principle of MOFs toward high-power and high-energy-density energy storage.

4. Experimental Section

Chemicals: All chemicals were purchased from commercial sources and used without further purification.

Synthesis of Co_4-Ir MOF: The cluster-bridging-coordinated bimetallic Co_4-Ir MOF was prepared by the solvothermal reaction of $Co(NO_3)_2{\cdot}6H_2O$ and Ir(ppy-COOH)$_3$ [ppy-COOH = 3-(pyridin-2-yl)benzoic acid] in a solution of DMF/H_2O/HCl. Ir(ppy-COOH)$_3$ was prepared according to the literature.[42,43,45] $Co(NO_3)_2{\cdot}6H_2O$ (0.05 mmol) dissolved in deionized water (2.0 mL) was added into a solution of Ir(ppy-COOH)$_3$ (0.015 mmol) dissolved in N,N'-dimethylformamide (DMF, 6.0 mL). The above solution was mixed with of HCl (12 mol L^{-1}, 23 µL) and heated at 120 °C for 48 h. The as-obtained green powder of Co_4-Ir MOF product was collected, washed with DMF and ethanol, and dried under vacuum for 24 h. The yield of Co_4-Ir MOF was 65%.

Material Characterizations: Powder X-ray diffraction (PXRD) spectroscopy was performed using a Bruker D8 ADVANCE X-ray powder diffractometer with a Cu Kα radiation source (λ = 1.54056 Å). The morphology of the samples was analyzed using field-emission SEM (FEI Nova NanoSEM 450) at 5.0 kV with an attached EDX apparatus (Bruker Quantax-200). XPS analysis was conducted on a PHI-5000 Versa Probe X-ray photoelectron spectrometer using an Al Kα X-ray source. Infrared spectra were measured on a Bruker Tensor 27 spectrometer using KBr-mixed pellets in the range of 400–4000 cm^{-1}. Thermogravimetric analysis (TGA) was performed under N_2 flow in a temperature range of 25–500 °C at a heating rate of 5 °C min^{-1} on a Mettler Toledo TGA/DSC-1 instrument. N_2 adsorption/desorption isotherms were measured using a BELSORP-max instrument (BEL Japan, Inc.) at 77 K. In the conductivity test, the MOF powder was pressed in a mold with a diameter of 4 mm and a thickness of 2 mm under a pressure of 1 MPa. A four-probe method was applied with stainless steel electrodes using a Keithley 6430 source measurement unit. The bulk conductivity (κ) was calculated according to the following equation

$$\kappa = L/(R \times A) \tag{3}$$

where L and A are the thickness and sectional area of the pressed sample, respectively.

Electrochemical Measurements: To prepare the Co_4-Ir MOF anodes, Co_4-Ir MOF powder was mixed with conductive carbon black additive (Ketjen Black) and polytetrafluoroethylene (PVDF) binder (at a mass ratio of 7:1.5:1.5) in N-methyl-2-pyrrolidone (NMP). After stirring for 6 h, the homogeneous slurry was coated on a copper foil, dried under vacuum at 100 °C overnight, and then cut into circular disks (1.54 cm^2). It shall be noticed that the adsorbed water and solvents in Co_4-Ir MOF crystal have been completely removed at the temperature of 100 °C under vacuum. The $LiNi_{0.5}Co_{0.2}Mn_{0.3}O_2$ (NCM523) cathodes were prepared by mixing NCM523, Ketjen Black and PVdF-HFP at a mass ratio of 8:1:1 in NMP. After stirring for 6 h, the slurry was coated on a carbon-coated aluminum foil and dried under vacuum at 100 °C overnight and then cut into circular disks (1.54 cm^2). The coin cells (CR2032) were assembled in an argon-filled glove box with Celgard 2400 separators and an electrolyte of 1.0 mol L^{-1} $LiPF_6$ in ethylene carbonate/ethyl methyl carbonate/diethyl carbonate mixture (EC/EMC/DEC, 4:3:3, v/v/v) with 1 wt% vinylene carbonate (VC) additive. For Co_4-Ir MOF||Li half cells, the Co_4-Ir MOF anodes

were used as working electrodes, and lithium foils were used as the counter electrodes. The areal mass loading of Co_4-Ir MOF in the electrode was 2.0 mg cm^{-2}.

For the assembly of Co_4-Ir MOF||NCM523 full batteries, the Co_4-Ir MOF anodes were first prelithiated by dropwise adding 100 μL of electrolyte and then directly contacting a piece of lithium foil for 24 h in an Ar-filled glovebox. The NCM523 and prelithiated MOF anodes were used as the cathode material and anode material, respectively. The areal mass loadings of NCM523 cathodes and Co_4-Ir MOF anodes (with diameters of 14 mm) were 2.6 and 1.5 mg cm^{-2}, respectively.

For the assembly of Co_4-Ir MOF||AC HLICs, the AC and prelithiated Co_4-Ir MOF were used as the cathode material and anode material, respectively. The areal mass loadings of AC cathodes and Co_4-Ir MOF anodes (with diameters of 14 mm) were 2.5 and 0.5 mg cm^{-2}, respectively.

The resulting batteries were loaded into a Chenhua CHI-760e electrochemical workstation for CV and EIS measurements. EIS measurements were carried out in the range of 100 kHz to 0.01 Hz with an amplitude of 5 mV. The cycling stability and rate performances of batteries were measured on a LAND CT2001A analyzer at different current densities. The specific capacities of the batteries were calculated according to the loading mass of Co_4-Ir MOF. The specific capacitance (C) was calculated according to the following equation

$$C = (i \times t)/(\Delta V \times m) \quad (4)$$

where i is the current, t is the discharge time, ΔV is the voltage range (2 V), and m is the total mass of the AC cathode and Co_4-Ir MOF anode.

Supporting Information

Supporting Information is available from the Wiley Online Library or from the author.

Acknowledgements

W.Y. and K.F. contributed equally to this work. This work was supported by the National Key Research and Development Program of China (2017YFA0208200), the Fundamental Research Funds for the Central Universities of China (0205-14380266), the National Natural Science Foundation of China (22022505, 21872069, 21731003), the Natural Science Foundation of Jiangsu Province (BK20180008), and the Shenzhen Fundamental Research Program of Science, Technology and Innovation Commission of Shenzhen Municipality (JCYJ20180307155007589).

Conflict of Interest

The authors declare no conflict of interest.

Data Availability Statement

The data that support the findings of this study are available from the corresponding author upon reasonable request.

Keywords

anode materials, conductivity, hybrid lithium-ion capacitors, lithium-ion batteries, metal−organic framework

Received: July 25, 2021
Revised: October 9, 2021
Published online: October 29, 2021

[1] J.-M. Tarascon, M. Armand, *Nature* **2001**, *414*, 359.
[2] M. Armand, J.-H. Tarascon, *Nature* **2008**, *451*, 652.
[3] H. Liu, Z. Zhu, Q. Yan, S. Yu, X. He, Y. Chen, R. Zhang, L. Ma, T. Liu, M. Li, R. Lin, Y. Chen, Y. Li, X. Xing, Y. Choi, L. Gao, H. S.-Y. Cho, K. An, J. Feng, R. Kostecki, K. Amine, T. Wu, J. Lu, H. L. Xin, S. P. Ong, P. Liu, *Nature* **2020**, *585*, 63.
[4] H. Jin, S. Xin, C. Chuang, W. Li, H. Wang, J. Zhu, H. Xie, T. Zhang, Y. Wan, Z. Qi, W. Yan, Y.-R. Lu, T.-S. Chan, X. Wu, J. B. Goodenough, H. Ji, X. Duan, *Science* **2020**, *370*, 192.
[5] V. Etacheri, R. Marom, R. Elazari, G. Salitra, D. Aurbach, *Energy Environ. Sci.* **2011**, *4*, 3243.
[6] Y. Liu, G. Zhou, K. Liu, Y. Cui, *Acc. Chem. Res.* **2017**, *50*, 2895.
[7] Y. Yang, Y. Liu, K. Pu, X. Chen, H. Tian, M. Gao, M. Zhu, H. Pan, *Adv. Funct. Mater.* **2017**, *27*, 1605011.
[8] G. Zhu, L. Wang, H. Lin, L. Ma, P. Zhao, Y. Hu, T. Chen, R. Chen, Y. Wang, Z. Tie, J. Liu, Z. Jin, *Adv. Funct. Mater.* **2018**, *28*, 1800003.
[9] J. Shan, Y. Liu, P. Liu, Y. Huang, Y. Su, D. Wu, X. Feng, *J. Mater. Chem. A* **2015**, *3*, 24148.
[10] Y. Liu, Y. Takeda, T. Matsumura, J. Yang, N. Imanishi, A. Hirano, O. Yamamoto, *J. Electrochem. Soc.* **2006**, *153*, A437.
[11] H. J. Kim, S. Choi, S. J. Lee, M. W. Seo, J. G. Lee, E. Deniz, Y. J. Lee, E. K. Kim, J. W. Choi, *Nano Lett.* **2016**, *16*, 282.
[12] B. Zhu, G. Liu, G. Lv, Y. Mu, Y. Zhao, Y. Wang, X. Li, P. Yao, Y. Deng, Y. Cui, J. Zhu, *Sci. Adv.* **2019**, *5*, eaax0651.
[13] M. Chen, B. Li, X. Liu, L. Zhou, L. Yao, J. Zai, X. Qian, X. Yu, *J. Mater. Chem. A* **2018**, *6*, 3022.
[14] C. Cao, I. I. Abate, E. Sivonxay, B. Shyam, C. Jia, B. Moritz, T. P. Devereaux, K. A. Persson, H.-G. Steinrück, M. F. Toney, *Joule* **2019**, *3*, 762.
[15] Y. P. Wu, E. Rahm, R. Holze, *J. Power Sources* **2003**, *114*, 228.
[16] Y. Luan, J. Yin, K. Zhu, K. Cheng, J. Yan, K. Ye, G. Wang, D. Cao, *Chem. Eng. J.* **2020**, *392*, 123668.
[17] S. M. Jafari, M. Khosravi, M. Mollazadeh, *Electrochim. Acta* **2016**, *203*, 9.
[18] J. Xiao, M. Yao, K. Zhu, D. Zhang, S. Zhao, S. Lu, B. Liu, W. Cui, B. Liu, *Nanoscale* **2013**, *5*, 11306.
[19] X. Zuo, J. Zhu, P. Müller-Buschbaum, Y.-J. Cheng, *Nano Energy* **2017**, *31*, 113.
[20] Y. Lu, L. Yu, X. W. D. Lou, *Chem* **2018**, *4*, 972.
[21] O. M. Yaghi, *ACS Cent. Sci.* **2019**, *5*, 1295.
[22] N. Ogihara, T. Yasuda, Y. Kishida, T. Ohsuna, K. Miyamoto, N. Ohba, *Angew. Chem., Int. Edit.* **2014**, *53*, 11467.
[23] P. Xiong, G. Zeng, L. Zeng, M. Wei, *Dalton Trans.* **2015**, *44*, 16746.
[24] S. Maiti, A. Pramanik, U. Manju, S. Mahanty, *Micropor. Mesopor. Mat.* **2016**, *226*, 353.
[25] C. Li, X. Lou, L. Zhang, Y. Wang, J.-P. Amoureux, M. Shen, Q. Chen, B. Hu, *J. Mater. Chem. A* **2016**, *4*, 16245.
[26] Q. Liu, L. Yu, Y. Wang, Y. Ji, J. Horvat, M.-L. Cheng, X. Jia, G. Wang, *Inorg. Chem.* **2013**, *52*, 2817.
[27] Q. Huang, T. Wei, M. Zhang, L.-Z. Dong, A.-M. Zhang, S.-L. Li, W.-J. Liu, J. Liu, Y.-Q. Lan, *J. Mater. Chem. A* **2017**, *5*, 8477.
[28] D. Zhou, J. Ni, L. Li, *Nano Energy* **2019**, *57*, 711.
[29] Y. Ozawa, N. Ogihara, M. Hasegawa, O. Hiruta, N. Ohba, Y. Kishida, *Commun. Chem.* **2018**, *1*, 65.
[30] W. Yan, J. Su, Z.-M. Yang, S. Lv, Z. Jin, J.-L. Zuo, *Small* **2020**, *17*, 2005209.
[31] X. Lou, Y. Ning, C. Li, X. Hu, M. Shen, B. Hu, *Sci. China Mater.* **2018**, *61*, 1040.
[32] C. Li, L. Liu, J. Kang, Y. Xiao, Y. Feng, F.-F. Cao, H. Zhang, *Energy Storage Mater.* **2020**, *31*, 115.
[33] S. Sanati, R. Abazari, J. Albero, A. Morsali, H. García, Z. Liang, R. Zou, *Angew. Chem., Int. Edit.* **2021**, *60*, 11048.
[34] M. Wang, R. Dong, X. Feng, *Chem. Soc. Rev.* **2021**, *50*, 2764.

[35] K. Wada, K. Sakaushi, S. Sasaki, H. Nishihara, *Angew. Chem., Int. Edit.* **2018**, *57*, 8886.
[36] C. Zhang, K. Fan, Y. Chen, Y. Wu, C. Wang, *ACS Appl. Electron. Mater.* **2021**, *3*, 1947.
[37] M. Wang, H. Shi, P. Zhang, Z. Liao, M. Wang, H. Zhong, F. Schwotzer, A. S. Nia, E. Zschech, S. Zhou, S. Kaskel, R. Dong, X. Feng, *Adv. Funct. Mater.* **2020**, *30*, 2002644.
[38] Y. Chen, M. Tang, Y. Wu, X. Su, X. Li, S. Xu, S. Zhuo, J. Ma, D. Yuan, C. Wang, W. Hu, *Angew. Chem., Int. Ed.* **2019**, *58*, 14731.
[39] Y. Wu, Y. Chen, M. Tang, S. Zhu, C. Jiang, S. Zhuo, C. Wang, *Chem. Commun.* **2019**, *55*, 10856.
[40] K. Fan, C. Zhang, Y. Chen, Y. Wu, C. Wang, *Chem* **2021**, *7*, 1224.
[41] K. Fan, C. Zhang, Y. Chen, G. Zhang, Y. Wu, J. Zuo, C. Wang, *J. Mater. Chem. C* **2021**, https://doi.org/10.1039/D1TC03709A.
[42] K. Fan, W.-X. Nie, L.-P. Wang, C.-H. Liao, S.-S. Bao, L.-M. Zheng, *Chem. Eur. J.* **2017**, *23*, 6615.
[43] C.-H. Liao, K. Fan, S.-S. Bao, H. Fan, X.-Z. Wang, Z. Hu, M. Kurmoo, L.-M. Zheng, *Chem. Commun.* **2019**, *55*, 13920.
[44] Q.-R. Fang, D.-Q. Yuan, J. Sculley, J.-R. Li, Z.-B. Han, H.-C. Zhou, *Inorg. Chem.* **2010**, *49*, 11637.
[45] Z. Xie, L. Ma, K. E. deKrafft, A. Jin, W. Lin, *J. Am. Chem. Soc.* **2010**, *132*, 922.
[46] M. Armand, S. Grugeon, H. Vezin, S. Laruelle, P. Ribière, P. Poizot, J.-M. Tarascon, *Nat. Mater.* **2009**, *8*, 120.
[47] Y. Hua, X. Li, C. Chen, H. Pang, *Chem. Eng. J.* **2019**, *370*, 37.
[48] S. Li, J. Lin, W. Xiong, X. Guo, D. Wu, Q. Zhang, Q.-L. Zhu, L. Zhang, *Coord. Chem. Rev.* **2021**, *438*, 213872.
[49] L. Sun, T. Miyakai, S. Seki, M. Dincă, *J. Am. Chem. Soc.* **2013**, *135*, 8185.
[50] Y. Zhang, S. N. Riduan, J. Wang, *Chem. Eur. J.* **2017**, *23*, 16419.
[51] W. Xia, A. Mahmood, R. Zou, Q. Xu, *Energy. Environ. Sci.* **2015**, *8*, 1837.
[52] X. Han, G. Qing, J. Sun, T. Sun, *Angew. Chem., Int. Edit.* **2012**, *51*, 5147.
[53] Y. Lu, X. Hou, L. Miao, L. Li, R. Shi, L. Liu, J. Chen, *Angew. Chem., Int. Edit.* **2019**, *58*, 7020.
[54] J. Wang, J. Polleux, J. Lim, B. Dunn, *J. Phys. Chem. C* **2007**, *111*, 14925.
[55] J. Wu, X. Rui, C. Wang, W.-B. Pei, R. Lau, Q. Yan, Q. Zhang, *Adv. Energy Mater.* **2015**, *5*, 1402189.
[56] Z. Lei, Q. Yang, Y. Xu, S. Guo, W. Sun, H. Liu, L.-P. Lv, Y. Zhang, Y. Wang, *Nat. Commun.* **2018**, *9*, 576.
[57] Y. Chen, Q. Zhu, K. Fan, Y. Gu, M. Sun, Z. Li, C. Zhang, Y. Wu, Q. Wang, S. Xu, J. Ma, C. Wang, W. Hu, *Angew. Chem., Int. Edit.* **2021**, *60*, 18769.
[58] N. Ogihara, Y. Ozawa, O. Hiruta, *J. Mater. Chem. A* **2016**, *4*, 3398.
[59] J. Sun, L. Guo, X. Sun, J. Zhang, Y. Liu, L. Hou, C. Yuan, *J. Mater. Chem. A* **2019**, *7*, 24788.
[60] H. Yang, S. Zhang, L. Han, Z. Zhang, Z. Xue, J. Gao, Y. Li, C. Huang, Y. Yi, H. Liu, Y. Li, *ACS Appl. Mater. Interfaces* **2016**, *8*, 5366.